catalysts

MDPI

Article

Green Synthesis of Iron Oxide Nanoparticles Using *Psidium guajava* L. Leaves Extract for Degradation of Organic Dyes and Anti-microbial Applications

Anup Adhikari [1], Kisan Chhetri [2], Debendra Acharya [2], Bishweshwar Pant [3,4,*] and Achyut Adhikari [1,*]

[1] Central Department of Chemistry, Tribhuvan University, Kirtipur, Kathmandu 44618, Nepal
[2] Department of Nano Convergence Engineering, Jeonbuk National University, Jeonju 561756, Korea
[3] Carbon Composite Energy Nanomaterials Research Center, Woosuk University, Wanju 55338, Korea
[4] Woosuk Institute of Smart Convergence Life Care (WSCLC), Woosuk University, Wanju 55338, Korea
* Correspondence: bisup@woosuk.ac.kr (B.P.); achyutraj05@gmail.com (A.A.)

Abstract: Among various metal and metal oxide nanoparticles, iron-oxide nanoparticles (IONPs) have been more widely used for the degradation of harmful organic dyes and the inhibition of microbial growth; on the other hand, it positively affects mammalian cells. Green synthesis of IONPs has piqued the interest of researchers because it improves stability and is an environmentally friendly method of avoiding the use of harmful chemicals as a reducing agent. In this study, IONPs were synthesized using *Psidium guajava* leaf extract, which was further applied for its industrial dye degradation and anti-microbial activities. UV–visible spectroscopy, FTIR, XRD, XPS, EDX, FE-SEM, HR-TEM, and Zeta potential analysis were used to characterize the synthesized nanoparticles. The synthesized IONPs managed to degrade methylene blue (MB) and methyl orange (MO) in the presence of H_2O_2. The degradation efficiency was 82.1% in 95 min and 53.9% in 205 min for MB and MO, respectively. Likewise, the synthesized IONPs showed good anti-bacterial activity with a ZOI of 13 mm for both *Shigella sonnei* and *Staphylococcus aureus* gram-positive bacteria. Similarly, they demonstrated good anti-fungal activity with ZOI of 15 mm and 13 mm for *Candida tropicalis* and *Candida albicans*, respectively. Thus, the IONPs can combat harmful organic dyes, and they can terminate the pathogenicity of several human pathogens.

Keywords: anti-microbial activity; dye degradation; green synthesis; iron oxide nanoparticles; *Psidium guajava*

Citation: Adhikari, A.; Chhetri, K.; Acharya, D.; Pant, B.; Adhikari, A. Green Synthesis of Iron Oxide Nanoparticles Using *Psidium guajava* L. Leaves Extract for Degradation of Organic Dyes and Anti-microbial Applications. *Catalysts* **2022**, *12*, 1188. https://doi.org/10.3390/catal12101188

Academic Editor: Maria Cornelia Iliuta

Received: 20 September 2022
Accepted: 6 October 2022
Published: 7 October 2022

1. Introduction

In the current scenario, the nanotechnology field is fledgling daily with paramount importance due to its new developments and wide range of applications. Metal nanoparticles with a high specific surface area and a high fraction of surface atoms have been extensively studied due to their unique physiochemical properties, which include electronic magnetic, catalytic, optical, anti-corrosion, and anti-microbial activities [1–4].

Magnetite (Fe_3O_4) and maghemite (γ-Fe_2O_3) have been the two most studied iron oxides [5]. Iron oxide nanoparticles (IONPs) are found in the environment naturally as particulate matter in air pollution and volcanic eruptions. Particles of Fe_3O_4 (magnetite) or γ-Fe_2O_3 (maghemite) can be generated as emissions from traffic, industry, and power plants, but they can also be chemically synthesized for a wide range of applications [6–8]. Magnetic behavior is an essential parameter in the design and synthesis of super-paramagnetic IONPs to maximize their application potential. Moreover, IONPs are easy to synthesize, low-cost, and versatile materials.

A green approach has received much attention for synthesizing metal oxide nanoparticles because of its convenience of use and underlying safety [9]. IONPs have sparked much interest recently, as they can be quickly recovered from reaction mixtures by applying

an external magnetic field. Although many chemical and physical synthesis methods are known, green synthesis is safer, more sustainable, and biologically acceptable. The primary biological materials used in the green synthesis are plants and microbes. Additionally, these biomaterials play the role of stabilizing, reducing, capping, and fabricating agents in the green synthesis of nanoparticles [10].

Psidium guajava (commonly known as guava) is a well-known tropic tree widely grown for its fruit. It is a member of the Magnoliophyta phylum, Magnoliopsida class, and Myrtaceae family [11]. *Psidium guajava* and its different parts have great medicinal value. Leaves and bark have a considerable content of anti-microbial and anti-bacterial compounds [12]. The stem's ethanolic extracts have potent anti-diabetic properties. Among the many antioxidants and phytochemicals found in guava are polysaccharides, minerals, essential oils, vitamins, and triterpenoid acid, including tannins, flavonoids, alkaloids, steroids, glycosides, and saponins [13]. Guava contains more vitamin C and A than other fruits, and guava also contains pectin, which is a type of dietary fiber. Current research focuses on the phytochemistry and medicinal value of *Psidium guajava* (guava) in light of its historical context, essential ingredients, and common uses [14].

IONPs are effective photocatalysts absorbing visible light. TiO_2, a frequently used photocatalyst due to its broad band-gap of 3.2 eV, absorbs UV light with wavelengths of 380 nm (covering just 5% of the solar spectrum). While Fe_2O_3, an intriguing n-type semiconducting material with a band-gap of 2.2 eV, is a good candidate for photodegradation under visible light conditions, making IONPs more effective than TiO_2 [15]. IONPs superior photocatalytic performance over TiO_2 can be due to the significant production of electron-hole pairs caused by the narrow band-gap irradiation [16]. Due to their enhanced photocatalytic action, various Fe (III) oxide species, including Fe_2O_3 and -FeOOH, have been proposed to degrade organic pollutants and lessen their toxicity [17]. IONPs can even be used for the adsorption of dyes [18]. IONPs are one of the potential materials for photocatalytic application [19] due to their narrow band gap [20], chemical stability, high surface area and absorbing light up to 600 nm, and effective electrons excitation of FeO from the valence band to the conduction band [21]. IONPs can act in Fenton processes as precursors of Fe ions and as photocatalysts under visible light since they have a lower band gap (2.2 eV) [22]. Hence, IONPs can be used as Fenton-like oxidants for degrading dyes like methylene blue and methyl orange (Figure 1). The photocatalytic degradation of dyes makes nanoparticles effective for bio-remediate use.

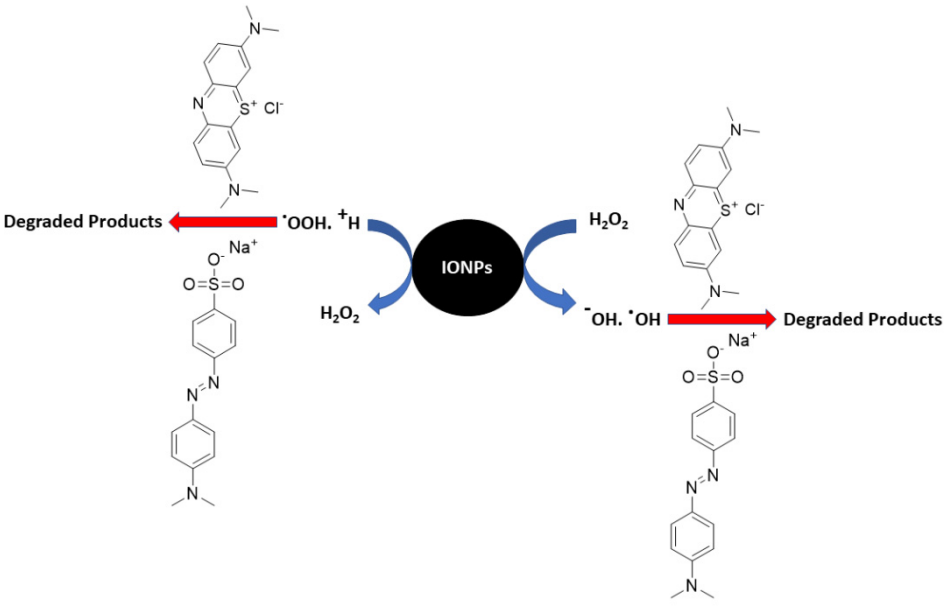

Figure 1. Mechanism of Fenton's process by IONPs in degradation of MB and MO.

The IONPs have found widespread use in a variety of biomedical fields. Iron is a key microelement that plays a vital role in the function of different hierarchies of living systems. The abundance of iron and its physiological functions call into question the ability of iron compounds at the same concentrations to inhibit microbial growth while positively affecting mammalian cells. Several studies have demonstrated the anti-microbial activity of IONPs against gram-negative and gram-positive bacteria and fungi. Several studies have shown that IONPs are not toxic to eukaryotic cells. It raises the prospect of IONPs being considered potential anti-microbial agents of the next generation, with anti-microbial activity and high biocompatibility with the human body [23]. Iron performs a variety of biological functions in living organisms. Despite its functions in living organisms, it can catalyze the Fenton reaction and reactive oxidation species (ROS) to damage DNA, lipids, and proteins [24–26].

Moreover, the presence of hydroxyl radicals in the Fenton system is also responsible for organic dye degradation. The hydroxyl radical generated by ferrite ion attacks organic dyes resulting in its degradation [27]. Likewise, IONPs exhibit anti-microbial activity by damaging bacterial cells through the same mechanisms. The ROS, in turn, has a genotoxic effect, causing DNA molecules to be damaged [25]. The ability of nanoparticles with small sizes to inhibit DNA replication by inactivating topoisomerase is also found in many cases [28]. IONPs are magnetic as well as paramagnetic. Super-paramagnetic IONPs are another name for Fe_3O_4 NPs with high paramagnetic activity. They cause cell death and biofilm destruction in the presence of alternating magnetic fields due to vibration damage, local hyperthermia, and ROS generation. All the above-mentioned factors result in bacterial dissociation from a biofilm, bacterial cell wall damage, membrane rupture, and death [23].

Herein, we report the green synthesis, dye degradation potential, and anti-microbial activities of biofunctionalized IONPs from *Psidium guajava* leaves extracts. Green synthesized IONPs dye degradation potential was studied for methylene blue and methyl orange. Similarly, the IONPs also showed good anti-bacterial activity in vitro against *Shigella sonnei*, and *Staphylococcus aureus* and good anti-fungal activity in vitro against *Candida tropicalis* and *Candida albicans*.

2. Results and Discussion

The color change immediately after adding the plant extract to the iron salt solution confirmed the formation of IONPs. In a matter of seconds, the color of the mixture changed from transparent yellow to black, demonstrating the synthesis of iron nanoparticles (Figure S1). The IONPs dark color was caused by surface plasmon excitation vibrations [29]. This was confirmed by the appearance of two absorption bands at about 255 nm and 328 nm (Figure 2a), which is very similar to what has previously been reported for IONPs [30,31].

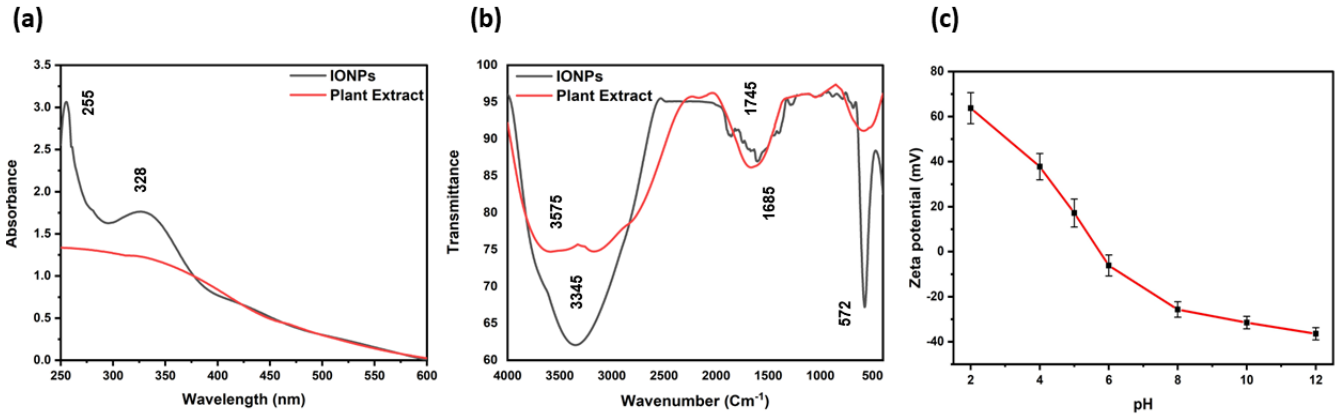

Figure 2. (**a**) UV–Vis spectrum of synthesized IONPs and plant extract, (**b**) FTIR spectra of synthesized IONPs and plant extract, and (**c**) Graph illustrating zeta potential vs. pH of biosynthesized IONPs.

The FTIR analysis of the synthesized sample (400–4000 cm^{-1}) confirmed the synthesis of IONPs and the presence of various reducing agent functional groups present in the plant extract (Figure 2b). The absorption peaks for IONPs were 572, 1745, and 3345 cm^{-1}, and for *Psidium guajava* extract were 1687 and 3575 cm^{-1}; these peaks were almost in line with prior literature [32]. The band at 3575 cm^{-1} is attributed to the O-H stretching vibration of alcohol and phenol compounds. In comparison, the bands at 1680–1750 cm^{-1} are attributed to the C=O stretching mode of carbonyl functional groups in ketone esters and acids [33]. During the formation of IONPs, the carbonyl band at 1687 cm^{-1} was shifted to 1745 cm^{-1}. The shift in bands at 1745 cm^{-1} indicated carboxylic acid coordination with IONPs, while 572 cm^{-1} is attributed to FeO, as reported in the literature [34].

The magnitude of zeta potential is an important parameter for explaining the stability of a colloidal nanostructure system, where a larger magnitude of negative or positive zeta potential indicates a stable suspension due to repulsive forces, which in turn depends on the nature of the dispersant, i.e., pH, as well as other factors such as conductivity and concentration [35]. Nanoparticles with zeta potentials greater than +30 mV or less than −30 mV are remarkably stable in the dispersion medium [36]. Figure 2c depicts the zeta potentials of IONPs at various pH values. The zeta potential indicates the dispersion stability of particles in colloids. The IONPs zeta potentials varied between 63.71 mV and −36.46 mV. The IONPs zeta potential decreased as the pH increased from two to eight, while the point of zero charges (PZC) was observed around pH five to six. These findings indicated particle aggregation would occur when the pH was near neutral, and these IONPs are stable at pH above 10. This result is coherent with previously reported works of the literature [37,38].

FE-SEM provided further insight into the morphology and size details of the IONPs. The morphology of the synthesized nanoparticle is shown in Figure 3a. The figure shows that the as-synthesized nanoparticles are not uniform and, in some cases, agglomerated. The large agglomerated clusters were formed due to the accumulation of tiny building blocks of various bioactive reducing agents in plant extract or as a result of the plant extract's lower capping ability and the agglomeration tendency of the iron-based nanoparticles due to magnetic interactions. The elemental composition of the sample was analyzed by EDX analysis. The EDX analysis in Figure 3b clearly shows the presence of the K-α at 6.4 keV due to Fe atoms present in the nanoparticle and K-α lines at 0.6 keV from O atoms. Similar results were also obtained by another study [39]. Other tiny peaks, such as K-α 0.25 keV, are due to adventitious carbon and oxygen that are commonly observed even without sample loading [40]. The percentage of weight present under the irradiated areas was 34.8% and 65.2% for oxygen, and iron, respectively.

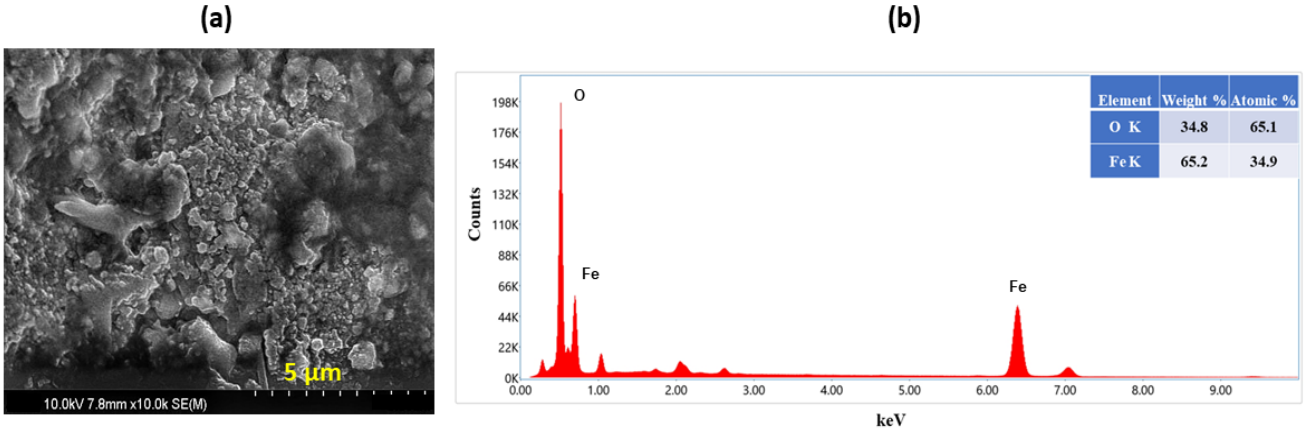

Figure 3. (**a**) FE-SEM images of biosynthesized IONPs at a magnification of 5 µm, (**b**) EDX spectrum of biosynthesized IONPs.

X-ray photoemission measurements were performed on the synthesized IONPs. Table S1 depicts the XPS data (BE, FWHM, area, atomic percentage, and assignments) collected at the C 1s, N 1s, O 1s, and Fe 2p core levels, which are the most indicative for the in-

terpretation. The XPS spectra of the synthesized product are shown in Figure 4a. The photoelectron peaks at 709.49 and 723.08 eV correspond to the binding energy of Fe^{2+} and Fe^{3+}, respectively (Figure 4b), and are consistent with the oxidation state of Fe in FeO and Fe_3O_4. Similarly, the deconvoluted 1s spectrum of oxygen demonstrated valuable information regarding the chemical states of oxygen linkage in IONPs. The photoelectron peak at 528.69 eV is comparable to that observed in the literature as X=O (where X can be any active component in the biomolecule) and may be a by-product generated during the biosynthesis of IONPs using *Psidium guajava* leaves extracts. The photoelectron peak at 530.46 eV is attributed to lattice oxygen (O in Fe-O-H), whereas the photoelectron peak at 534.62 eV corresponds to Fe-O (Figure 4c). These results resemble previous studies [41–44]. As XPS spectra can identify the interaction between plant extract and IONPs, the deconvoluted photoelectron peaks at 284.38 and 288.34 eV correspond to C-N and C=O, respectively, in C 1s spectrum (Figure 4e). Moreover, the deconvoluted photoelectron peaks at 398.38, 403.08, and 407.85 eV correspond to N-C, graphitic nitrogen, and cellulose nitrogen, respectively, in the N 1s spectrum (Figure 4d). This also indicates the chemical bonding of phytochemical elements to the IONP surface, and these results resemble previous works of literature [44,45]. Thus, IONPs were coated with phytochemical constituents obtained from plant extract, which is supported by this chelation demonstration.

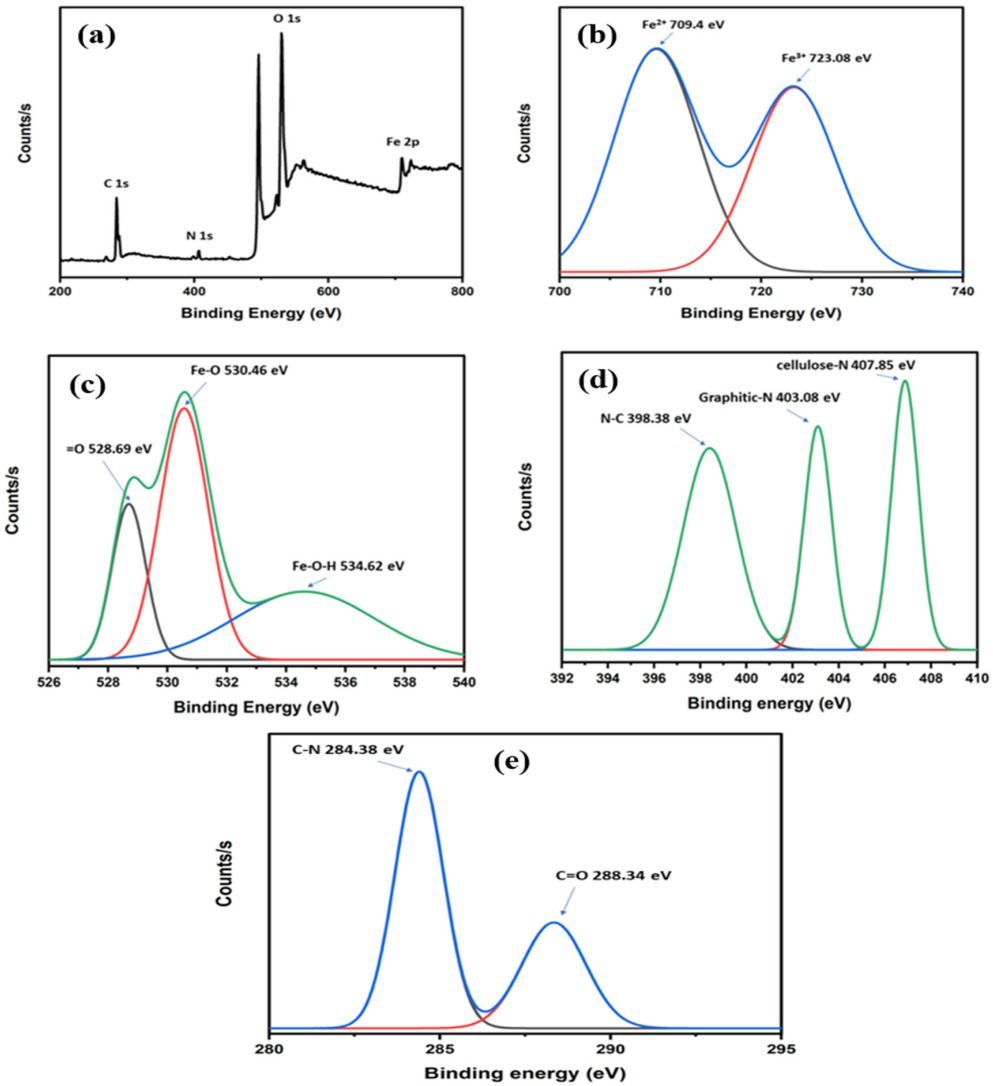

Figure 4. (**a**) XPS spectrum of biosynthesized IONPs, (**b**) Fe 2p spectra, (**c**) O 1s spectra, (**d**) N 1s spectra, and (**e**) C 1s spectra.

The crystalline structure of biosynthesized IONPs using a *Psidium guajava* extract was also confirmed by XRD analysis. The XRD pattern of the IONPs is shown in Figure 5a. The figure shows five distinct peaks at 2θ values of 31.68°, 32.56°, 35.15°, 45.46°, and 56.49° with corresponding lattice plane values at (111), (220), (311), (400), and (422), respectively. Furthermore, all these diffraction peaks are in good agreement with the database of standard JCPDS Card number 00-019-0629. Hence, this confirms the cubic crystallinity of the synthesized IONPs [46]. In addition to this, these values are consistent with the previously reported results [44,47]. Besides this, other characteristic peaks may be due to the crystalline nature of the bio-organic phase (capping agent) on the surface of IONPs. The average crystallite size was 21.75 nm using the Debye–Scherrer equation (Table S2).

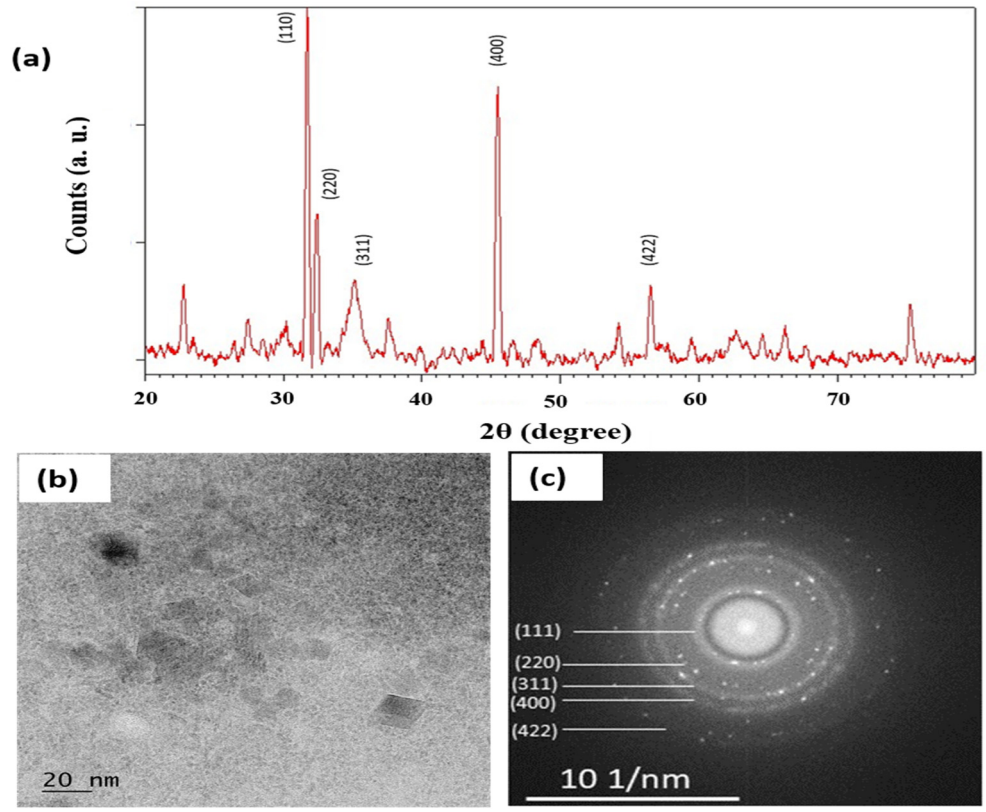

Figure 5. (**a**) XRD spectrum of biosynthesized IONPs and (**b**)TEM images of biosynthesized IONPs, and (**c**) SAED image.

Figure 5b depicts a TEM image of the synthesized IONPs. The grain size distribution was determined by taking the mean diameter of about 100 particles on the nano-graph. HR-TEM indicates the average grain size of nanoparticles to be 12.64 nm. The nanoparticles are almost cubic and partly spherical, which agrees with the above XRD analysis. Moreover, the selected area electron diffraction (SAED) pattern (Figure 5c) recorded from an area containing numerous nanoparticles reflects cubic crystallinity indexed as (111), (220), (311), (400), and (422), which is in agreement with XRD result as well. The given particle size obtained from the TEM analysis could be due to the nanoparticle's wide size distribution.

To decide if the synthesized IONPs can be utilized for the oxidative degradation of MB, the IONPs were utilized as the heterogeneous Fenton-like oxidants for the degradation of MB in an aqueous medium. The generation cycle of hydroxyl radicals in the Fenton system can be represented as below:

$$Fe^{2+} + H_2O_2 \rightarrow Fe^{3+} + OH^- + OH^{\bullet} \quad (1)$$

$$Fe^{3+} + H_2O_2 \rightarrow Fe^{2+} + H^+ + OOH^{\bullet} \quad (2)$$

Equations (1) and (2) show that ferrous ions initiate the reaction, resulting in the production of hydroxyl radicals, which then attack and degrade the MB [27]. Here are the generated $OH^{\bullet}$ radicals. Attack bonds in the MB might be in solution or sorbed on the IONPs surface. As mentioned in the literature, there will be no significant degradation with H_2O_2 alone [48,49]. However, when IONPs were added with H_2O_2, the color of MB vanished with a degradation efficiency of 82.1% after 95 min (Table S3). No significant changes were seen after 95 min. The red shift of the spectral band of MB occurred from 621 nm to 630 nm after incubating for 5 min in an aqueous solution of IONPs and H_2O_2 (Figure S2). This shift may be attributed to MB protonation [27]. MB was thus oxidized and decolorized via a Fenton-like reaction in which IONPs provided ferrous ions, leading to its degradation (Figure 6a). Similar results were obtained by Guidolin and co-workers [22], in which authors prepared IONPs by sol-gel method. Moreover, Ardakani and fellow researchers demonstrated that green-synthesized IONPs could show promising results for organic dye degradation [48].

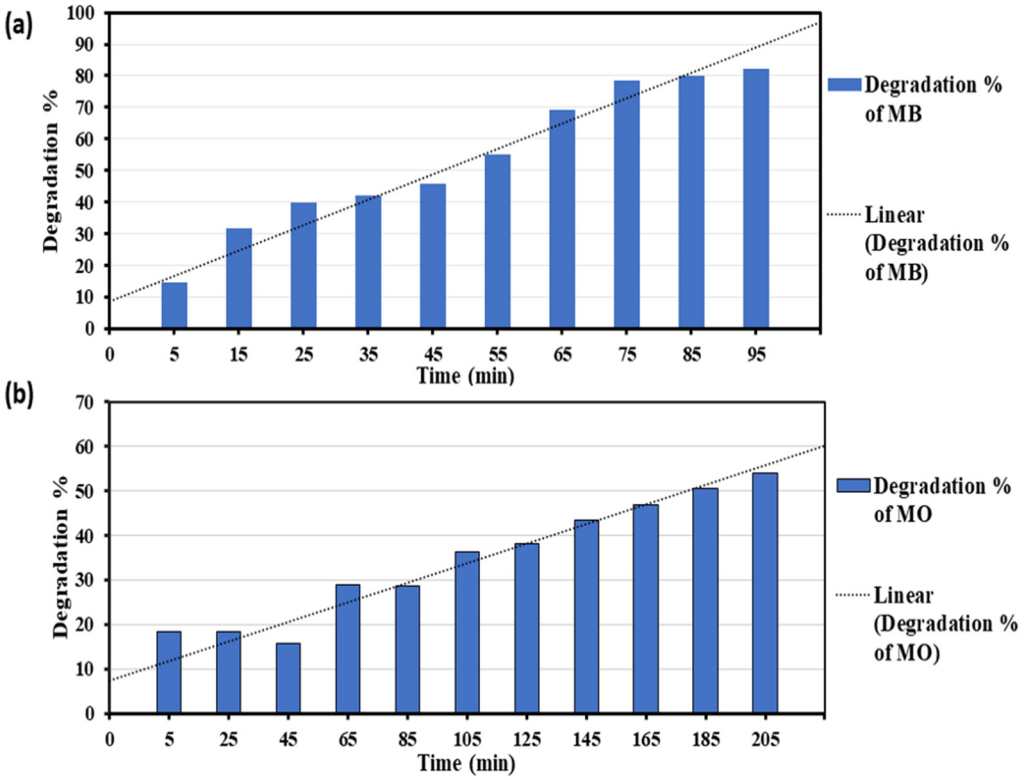

Figure 6. (**a**) Graphical representation of degradation of methylene blue and (**b**) Graphical representation of degradation of methyl orange.

In the similar manner mentioned above, synthesized IONPs were utilized for oxidative degradation of MO. The IONPs were utilized as the heterogeneous Fenton-like oxidants for the degradation of MO in an aqueous medium. When IONPs were added with H_2O_2, the color of MO vanished with a degradation efficiency of 53.94% after 205 min (Table S4). After 205 min, no appreciable change was observed. The red shift of the spectral band of MO occurred from 465 nm to 470 nm after incubating for 5 min in an aqueous solution of IONPs and H_2O_2 (Figure S3). This shift may be attributed to MO protonation and azonium ion formation [27]. MO can be oxidized and decolorized using a Fenton-like reaction with IONPs as a source of ferrous ions. A combination of IONPs and H_2O_2 can produce free hydroxyl radicals, as shown in Equations (1) and (2). These radicals can decompose MOs azo bond (-N=N-), resulting in the decolorization of dye-contaminated aqueous media [48]. MO was thus oxidized and decolorized, leading to its degradation (Figure 6b). It was found that MB degradation occurred at a faster rate than that of MO. The by-products during

the degradation of MO, i.e., azo bond (-N=N-), were more durable and harder to cleave, which is why they degraded at a slower than that of MB [50]. Our results were found to be coherent with previously reported research. Ardakani and fellow researchers demonstrated that green synthesized IONPs show a suitable catalyzing property in the degradation of methyl orange [48]. Muthukumar and Matheswaran demonstrated that green-synthesized IONPs show better MO degradation than chemically synthesized IONPs [51].

The anti-bacterial activity of IONPs was studied using the diffuse disc method against Gram-positive (*Staphylococcus aureus*) and Gram-negative bacteria (*Shigella sonnei* and *Escherichia coli*). The biosynthesized IONPs showed better anti-bacterial activity (based on the zone of inhibition) against *Staphylococcus aureus* and *Shigella sonnei* (Figure 7a). When comparing *Shigella sonnei* and *Staphylococcus aureus*, IONPs showed equal anti-bacterial activity, i.e., ZOI of 13 mm. However, in the case of *E. coli*, IONPs did not show anti-bacterial activity (Table S5) (Figure 7b). These findings agree with results reported elsewhere [52–54].

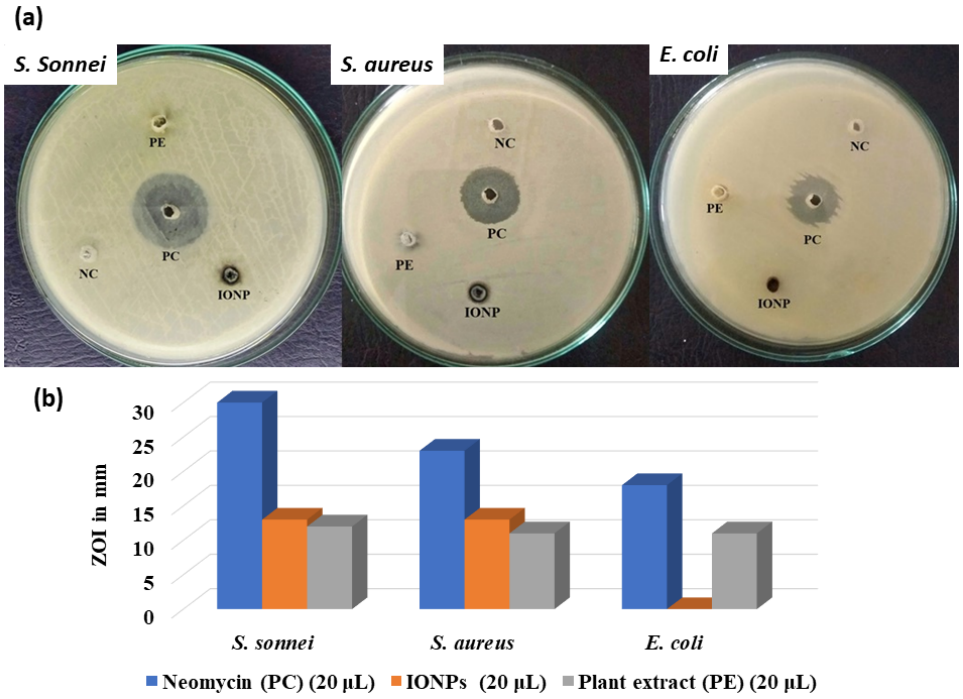

Figure 7. (**a**) Anti-bacterial activity of IONPs against *S. Sonnei*, *S. aureus*, and *E. coli* and (**b**) Comparative graphical representation of bacterial inhibition zone of IONPs on different bacterial strains.

The anti-fungal activity of IONPs was studied using the Agar Well Disc Diffusion method against *Candida tropicalis* and *Candida albicans*. The biosynthesized IONPs showed anti-fungal activity (based on the zone of inhibition) against *C. tropicalis* than *C. albicans* (Figure 8a). When comparing *C. tropicalis* and *C. albicans*, IONPs showed more anti-fungal activity, i.e., ZOI of 15 mm in the case of *C. tropicalis*, whereas, for *C. albicans*, it showed ZOI of 13 mm (Table S6) (Figure 8b). These findings hold good agreement with results published elsewhere [55,56]. Previous research has identified two possible mechanisms for the interaction of nanoparticles with bacteria and fungi. One of them is the increased production of reactive oxygen species (ROS), such as hydroxyl radical's percent (OH^-), singlet oxygen (O_2*), and hydrogen peroxide (H_2O_2) [57]. Electron-hole pairs are formed when IONPs with defects are activated by UV or visible light. The holes can split H_2O molecules into OH^- and H^+. Electron addition converts dissolved oxygen molecules to superoxide radical anions (O_2). The free radicals O_2^- and OH^- produced in the reactions can depolymerize polysaccharides, cause DNA strand breaks, initiate lipid peroxidation, and inactivate enzymes, leading to cell death [54]. Another plausible mechanism is nanoparticle binding to cell membrane proteins via electrostatic interactions, or nanoparticle accumula-

tion in the cytoplasm or periplasmic region, disrupting cellular function and membrane disruption and disorganization [54].

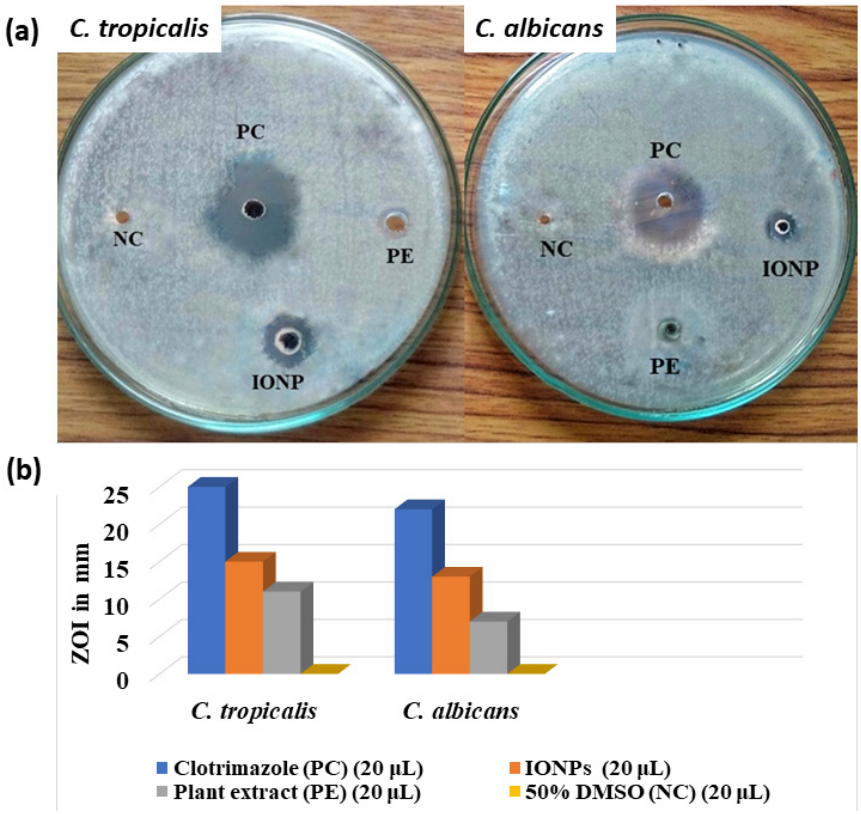

Figure 8. (**a**) Anti-fungal activity of IONPs against *C. tropicalis* and *C. albicans* and (**b**) Comparative graphical representation of fungicidal inhibition zone of IONPs on different fungal strains.

3. Materials and Methods

3.1. Plant Extract Preparation

The plant extract was prepared following our previously reported method [9]. In short, fresh leaves of *Psidium guajava* were collected from the open spaces of the Hetauda, Makawanpur District, with geographical distribution (27°40′31.96″ N, 85°07′13.31″ E). The collected leaf was rinsed adequately with running tap water, followed by distilled water, then dried at room temperature in the shade for two weeks. An electrical blender was used to grind the air-dried leaves into powder, and they were stored in polyethylene bags for future use. The leaf broth solution was prepared by adding 10 g of the final powder sample and 100 mL of distilled water. A magnetic stirrer stirred the solution at 60 °C for 45 min. After cooling, they were filtered through standard filter paper and Whatman Filter Paper No. 1. The filtrates were used for experiments, and the remaining extract was stored at 40 °C for further experiments.

3.2. Biosynthesis of Iron Oxide Nanoparticles

50 mL of the *Psidium guajava* leaves extract was added dropwise to $FeCl_2 \cdot 4H_2O$ and $FeCl_3 \cdot 6H_2O$ solutions (50 mL each), which were prepared considering a 1:2 molar ratio, respectively, at room temperature. Afterward, 1 M NaOH was added until the pH reached 11. After 30 min of stirring with a magnetic stirrer, the formation of a black-colored solution confirmed the synthesis of IONPs [58]. The nanoparticles were separated by centrifugation at 8000 rpm for 20 min and then washed 2–3 times with distilled water. Finally, the NPs were dried in a hot air oven at 80 °C for 3 h before being stored in a seal-tight container for future use. The synthetic protocol is given in Figure 9.

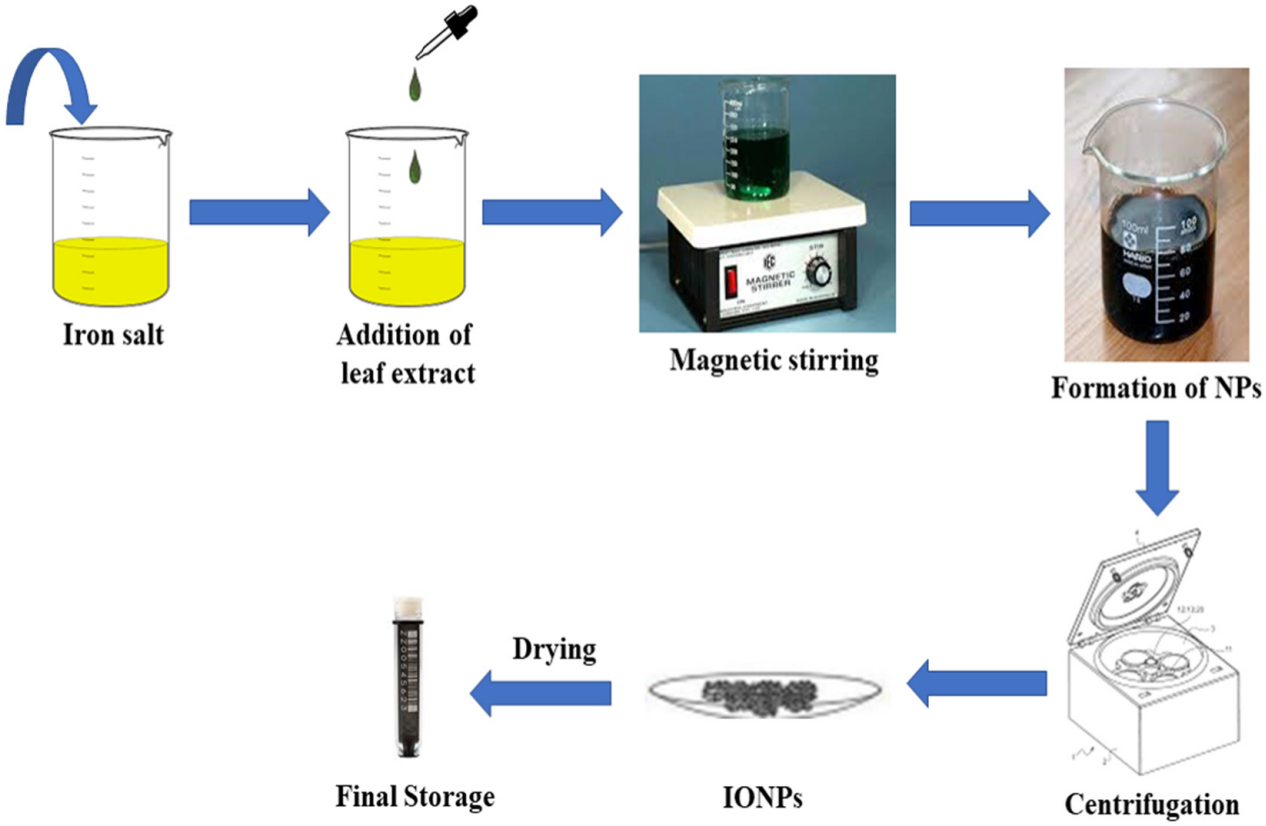

Figure 9. Schematic diagram showing the synthetic protocol for IONPs.

3.3. Dye Degradation Assay

The dye removal potential of IONPs was evaluated using methylene blue (MB) and methyl orange (MO) dyes. In a typical procedure, 25 mg of MB and MO were dissolved in 250 mL of distilled water to make a stock solution. Then, 20 mL of dye solution was ultrasonically mixed with 1 mg of IONPs and 0.5 mL of H_2O_2. Following that, 4 mL of each mixed solution was used at specific time intervals to assess the photocatalytic degradation of dye, i.e., in the presence of sunlight. A UV–Vis spectrophotometer was used to track the progress of the reaction by measuring the absorbance maxima of the resulting solution at different time intervals. The dye degradation efficiency was calculated as:

$$\text{Efficiency } (\%) = \frac{Ao - A}{Ao} \times 100$$

In this equation, efficiency (%) shows dye degradation efficiency, *Ao* denotes absorbance of dye solution at zero time, and *A* denotes absorbance of dye solution in suspension after time t [59].

3.4. Anti-microbial Activity of IONPs

The anti-microbial activities of IONPs resulting from the *Psidium guajava* extract were evaluated using the Agar Well Disc Diffusion Method [60]. For anti-bacterial analysis, the new culture of test organisms (*Shigella sonnei*, *Staphylococcus aureus*, and *Escherichia coli*) was spread on the MHA plate using a sterile cotton swab. IONPs (20 µL, 25 mg/500 µL), neomycin (1 mg/mL, positive control), and 50% DMSO (negative control) were all loaded separately onto the sterile blank anti-microbial susceptibility discs, which were later placed on the MHA plate and incubated at 37 °C for 18–24 h. After proper incubation, the zone of inhibition (ZOI) was measured, and the results were recorded.

Similarly, for anti-fungal analysis, the new culture of test organisms (*Candida tropicalis* and *Candida albicans*) was spread on the PDA plate using a sterile cotton swab. IONPs (20 µL,

25 mg/500 µL), clotrimazole (1 mg/mL, positive control), and 50% DMSO (negative control) were all loaded separately onto the sterile blank anti-microbial susceptibility discs, which were incubated at 37 °C for 18–24 h. After proper incubation, the zone of inhibition (ZOI) was measured, and the results were recorded.

4. Conclusions

The present study ascertained that using *Psidium guajava* extract as a reducing and capping agent in the green synthesis of IONPs has advantages, such as ease of availability, eco-friendliness, and economic viability. Secondary metabolites were in charge of green IONP synthesis. More research is required to pinpoint the precise mechanism and fathom the entire process of green IONP synthesis. Systematic characterization with UV–Vis, FTIR, XPS, XRD, FE-SEM, EDX, HR-TEM, and Zeta potential confirmed the green synthesis of IONPs using *Psidium guajava* extract. IONPs demonstrated excellent photocatalytic organic dye degradation efficiency of 82.1% and 53.9% in 95 min and 205 min for methylene blue and methyl orange. In vitro, the IONPs also demonstrated good anti-bacterial activity against *Shigella sonnei and Staphylococcus aureus*.

Similarly, it demonstrated good anti-fungal activity in vitro against *Candida tropicalis* and *Candida albicans*, paving the way for topical administration against these bacteria and fungi infections. Organic dyes produce hazardous defects that can be nullified using IONPs. Furthermore, the leaves of *Psidium guajava* may be helpful in nanotechnology.

Supplementary Materials: The following supporting information can be downloaded at: https://www.mdpi.com/article/10.3390/catal12101188/s1, Chemicals and reagents, various characterization techniques for iron oxide nanoparticles (UV–Vis Spectroscopy, Fourier Transform Infra-Red (FTIR), X-ray Diffraction (XRD), X-ray Photoelectron Spectroscopy (XPS), Scanning Electron Microscope (SEM), Transmission Electron Microscopy, Zeta potential analysis, Figure S1: Visible color change illustrating the formation of IONPs, Figure S2: UV–Vis absorption of methylene blue at a different time in presence of IONPs, Figure S3: UV–Vis absorption of methyl orange at a different time in presence of IONPs, Table S1: Binding energy, full width at half maxima, peak area and atomic percentage of synthesized IONPs sample, Table S2: Calculation of average crystallite size biosynthesized IONPs using XRD, Table S3: Calculation of methylene blue dye degradation efficiency by synthesized IONPs, Table S4: Calculation of methyl orange dye degradation efficiency by synthesized IONPs, Table S5: Anti-bacterial activity measured in terms of zone of inhibition (ZOI) of green synthesized IONPs, and Table S6: Anti-fungal activity measured in terms of zone of inhibition (ZOI) of green synthesized IONPs.

Author Contributions: Conceptualization, A.A. (Achyut Adhikari); data curation, A.A. (Anup Adhikari), K.C., D.A. and B.P.; formal analysis, A.A. (Anup Adhikari); Funding acquisition, A.A. (Anup Adhikari) and A.A. (Achyut Adhikari); investigation, A.A. (Achyut Adhikari), K.C., D.A. and B.P.; project administration, A.A. (Achyut Adhikari); resources, A.A. (Achyut Adhikari); supervision, B.P. and A.A. (Achyut Adhikari); validation, B.P. and A.A. (Achyut Adhikari); visualization, A.A. (Anup Adhikari), K.C. and D.A.; writing—original draft, A.A. (Anup Adhikari), D.A. and K.C.; writing—review and editing, A.A. (Anup Adhikari), K.C., B.P. and A.A. (Achyut Adhikari). All authors have read and agreed to the published version of the manuscript.

Funding: We thank the University Grant Commission (UGC), Nepal, for partial funding of the Master thesis of Anup Adhikari (Award no.: MRS-77/78-S&T-35).

Data Availability Statement: Not applicable.

Acknowledgments: We would like to thank the Department of Nano Convergence Engineering, Jeonbuk National University, Jeonju, South Korea, for EDX, SEM, TEM, and XPS techniques and Tista Prasai Joshi of the National Academy of Science and Technology (NAST), Lalitpur, Nepal for zeta potential measurement.

Conflicts of Interest: The authors declare no conflict of interest.

References

1. Narayan, N.; Meiyazhagan, A.; Vajtai, R. Metal Nanoparticles as Green Catalysts. *Materials* **2019**, *12*, 3602. [CrossRef] [PubMed]
2. Naseem, T.; Durrani, T. The Role of Some Important Metal Oxide Nanoparticles for Wastewater and Antibacterial Applications: A Review. *Environ. Chem. Ecotoxicol.* **2021**, *3*, 59–75. [CrossRef]
3. Chapagain, A.; Acharya, D.; Das, A.K.; Chhetri, K.; Oli, H.B.; Yadav, A.P. Alkaloid of Rhynchostylis Retusa as Green Inhibitor for Mild Steel Corrosion in 1 M H_2SO_4 Solution. *Electrochem* **2022**, *3*, 211–224. [CrossRef]
4. Adhikari, A.; Bhattarai, B.R.; Aryal, A.; Thapa, N.; Kc, P.; Adhikari, A.; Maharjan, S.; Chanda, P.B.; Regmi, B.P.; Parajuli, N. Reprogramming Natural Proteins Using Unnatural Amino Acids. *RSC Adv.* **2021**, *11*, 38126–38145. [CrossRef] [PubMed]
5. Gupta, A.K.; Gupta, M. Cytotoxicity Suppression and Cellular Uptake Enhancement of Surface Modified Magnetic Nanoparticles. *Biomaterials* **2005**, *26*, 1565–1573. [CrossRef] [PubMed]
6. Faraji, A.H.; Wipf, P. Nanoparticles in Cellular Drug Delivery. *Bioorg. Med. Chem.* **2009**, *17*, 2950–2962. [CrossRef] [PubMed]
7. Karlsson, H.L.; Holgersson, Å.; Möller, L. Mechanisms Related to the Genotoxicity of Particles in the Subway and from Other Sources. *Chem. Res. Toxicol.* **2008**, *21*, 726–731. [CrossRef]
8. Wilson, J.; Murray, V.; Kettle, J.N. The July 2005 London Bombings: Environmental Monitoring, Health Risk Assessment and Lessons Identified for Major Incident Response. *Occup. Environ. Med.* **2009**, *66*, 642–643. [CrossRef]
9. Adhikari, A.; Lamichhane, L.; Adhikari, A.; Gyawali, G.; Acharya, D.; Baral, E.R.; Chhetri, K. Green Synthesis of Silver Nanoparticles Using Artemisia Vulgaris Extract and Its Application toward Catalytic and Metal-Sensing Activity. *Inorganics* **2022**, *10*, 113. [CrossRef]
10. Priya; Naveen; Kaur, K.; Sidhu, A.K. Green Synthesis: An Eco-Friendly Route for the Synthesis of Iron Oxide Nanoparticles. *Front. Nanotechnol.* **2021**, *3*, 6555062.
11. Dakappa, S.S.; Adhikari, R.; Timilsina, S.S.; Sajjekhan, S. A Review on the Medicinal Plant *Psidium guajava* Linn. (Myrtaceae). *J. Drug Deliv. Ther.* **2013**, *3*, 2. [CrossRef]
12. Rahim, N.; Gomes, D.J.; Watanabe, H.; Rahman, S.R.; Chomvarin, C.; Endtz, H.P.; Alam, M. Antibacterial Activity of *Psidium guajava* Leaf and Bark against Multidrug-Resistant Vibrio Cholerae: Implication for Cholera Control. *Jpn J. Infect. Dis.* **2010**, *63*, 271–274. [CrossRef] [PubMed]
13. Smith, R.M.; Siwatibau, S. Sesquiterpene Hydrocarbons of Fijian Guavas. *Phytochemistry* **1975**, *14*, 2013–2015. [CrossRef]
14. Naseer, S.; Hussain, S.; Naeem, N.; Pervaiz, M.; Rahman, M. The Phytochemistry and Medicinal Value of *Psidium guajava* (Guava). *Clin. Phytosci.* **2018**, *4*, 32. [CrossRef]
15. Akhavan, O.; Azimirad, R. Photocatalytic Property of Fe_2O_3 Nanograin Chains Coated by TiO_2 Nanolayer in Visible Light Irradiation. *Appl. Catal. A Gen.* **2009**, *369*, 77–82. [CrossRef]
16. Bandara, J.; Klehm, U.; Kiwi, J. Raschig Rings-Fe_2O_3 Composite Photocatalyst Activate in the Degradation of 4-Chlorophenol and Orange II under Daylight Irradiation. *Appl. Catal. B Environ.* **2007**, *76*, 73–81. [CrossRef]
17. Feng, W.; Nansheng, D.; Helin, H. Degradation Mechanism of Azo Dye C. I. Reactive Red 2 by Iron Powder Reduction and Photooxidation in Aqueous Solutions. *Chemosphere* **2000**, *41*, 1233–1238. [CrossRef]
18. Xu, P.; Zeng, G.M.; Huang, D.L.; Feng, C.L.; Hu, S.; Zhao, M.H.; Lai, C.; Wei, Z.; Huang, C.; Xie, G.X.; et al. Use of Iron Oxide Nanomaterials in Wastewater Treatment: A Review. *Sci. Total Environ.* **2012**, *424*, 1–10. [CrossRef]
19. Jaafar, N.F.; Abdul Jalil, A.; Triwahyono, S.; Muhd Muhid, M.N.; Sapawe, N.; Satar, M.A.H.; Asaari, H. Photodecolorization of Methyl Orange over α-Fe_2O_3-Supported HY Catalysts: The Effects of Catalyst Preparation and Dealumination. *Chem. Eng. J.* **2012**, *191*, 112–122. [CrossRef]
20. Bakardjieva, S.; Stengl, V.; Subrt, J.; Houskova, V.; Kalenda, P. Photocatalytic Efficiency of Iron Oxides: Degradation of 4-Chlorophenol. *J. Phys. Chem. Sol.* **2007**, *68*, 721–724. [CrossRef]
21. Umar, A.; Akhtar, M.S.; Dar, G.N.; Baskoutas, S. Low-Temperature Synthesis of α-Fe_2O_3 Hexagonal Nanoparticles for Environmental Remediation and Smart Sensor Applications. *Talanta* **2013**, *116*, 1060–1066. [CrossRef] [PubMed]
22. Guidolin, T.; Possolli, N.M.; Polla, M.B.; Wermuth, T.B.; Franco de Oliveira, T.; Eller, S.; Klegues Montedo, O.R.; Arcaro, S.; Cechinel, M.A.P. Photocatalytic Pathway on the Degradation of Methylene Blue from Aqueous Solutions Using Magnetite Nanoparticles. *J. Clean. Prod.* **2021**, *318*, 128556. [CrossRef]
23. Gudkov, S.V.; Burmistrov, D.E.; Serov, D.A.; Rebezov, M.B.; Semenova, A.A.; Lisitsyn, A.B. Do Iron Oxide Nanoparticles Have Significant Antibacterial Properties? *Antibiotics* **2021**, *10*, 884. [CrossRef]
24. AlMatar, M.; Makky, E.A.; Var, I.; Koksal, F. The Role of Nanoparticles in the Inhibition of Multidrug-Resistant Bacteria and Biofilms. *Curr. Drug Deliv.* **2018**, *15*, 470–484. [CrossRef] [PubMed]
25. Groiss, S.; Selvaraj, R.; Varadavenkatesan, T.; Vinayagam, R. Structural Characterization, Antibacterial and Catalytic Effect of Iron Oxide Nanoparticles Synthesised Using the Leaf Extract of Cynometra Ramiflora. *J. Mol. Struct.* **2017**, *1128*, 572–578. [CrossRef]
26. Kohanski, M.A.; DePristo, M.A.; Collins, J.J. Sublethal Antibiotic Treatment Leads to Multidrug Resistance via Radical-Induced Mutagenesis. *Mol. Cell* **2010**, *37*, 311–320. [CrossRef] [PubMed]
27. Shahwan, T.; Abu Sirriah, S.; Nairat, M.; Boyacı, E.; Eroğlu, A.E.; Scott, T.B.; Hallam, K.R. Green Synthesis of Iron Nanoparticles and Their Application as a Fenton-like Catalyst for the Degradation of Aqueous Cationic and Anionic Dyes. *Chem. Eng. J.* **2011**, *172*, 258–266. [CrossRef]
28. Guittat, L.; Alberti, P.; Rosu, F.; Van Miert, S.; Thetiot, E.; Pieters, L.; Gabelica, V.; De Pauw, E.; Ottaviani, A.; Riou, J.-F.; et al. Interactions of Cryptolepine and Neocryptolepine with Unusual DNA Structures. *Biochimie* **2003**, *85*, 535–547. [CrossRef]

29. Devatha, C.P.; Thalla, A.K.; Katte, S.Y. Green Synthesis of Iron Nanoparticles Using Different Leaf Extracts for Treatment of Domestic Waste Water. *J. Clean. Prod.* **2016**, *139*, 1425–1435. [CrossRef]
30. Da'na, E.; Taha, A.; Afkar, E. Green Synthesis of Iron Nanoparticles by Acacia Nilotica Pods Extract and Its Catalytic, Adsorption, and Antibacterial Activities. *Appl. Sci.* **2018**, *8*, 1922. [CrossRef]
31. Jamzad, M.; Kamari Bidkorpeh, M. Green Synthesis of Iron Oxide Nanoparticles by the Aqueous Extract of Laurus Nobilis L. Leaves and Evaluation of the Antimicrobial Activity. *J. Nanostruct. Chem.* **2020**, *10*, 193–201. [CrossRef]
32. Somchaidee, P.; Tedsree, K. Green Synthesis of High Dispersion and Narrow Size Distribution of Zero-Valent Iron Nanoparticles Using Guava Leaf (*Psidium guajava* L.) Extract. *Adv. Nat. Sci. Nanosci. Nanotechnol.* **2018**, *9*, 035006. [CrossRef]
33. Bellamy, L.J. *The Infra-Red Spectra of Complex Molecules*; Springer: Dordrecht, The Netherlands, 1975; ISBN 978-94-011-6017-9.
34. Sundari, J.J.; Praba, P.; Brightson, Y.; Brightson Arul Jacob, Y.; Vasantha, V.; Shanmugaiah, V. Green Synthesis and Characterization of Zero Valent Iron Nanoparticles from the Leaf Extract of *Psidium guajava* Plant and Their Antibacterial Activity. *Chem. Sci. Rev. Lett.* **2017**, *2017*, 1244–1252.
35. Khatri, M.; Gupta, A.; Gyawali, K.; Adhikari, A.; Koirala, A.R.; Parajuli, N. Photocatalytic Degradation of Dyes Using Synthesized δ-MnO_2 Nanostructures. *Chem. Data Collect.* **2022**, *39*, 100854. [CrossRef]
36. dos Santos, K.C.; da Silva, M.F.G.; Pereira-Filho, E.R.; Fernandes, J.B.; Polikarpov, I.; Forim, M.R. Polymeric Nanoparticles Loaded with the 3,5,3′-Triiodothyroacetic Acid (Triac), a Thyroid Hormone: Factorial Design, Characterization, and Release Kinetics. *Nanotechnol. Sci. Appl.* **2012**, *5*, 37–48. [CrossRef]
37. Meng, X.; Ryu, J.; Kim, B.; Ko, S. Application of Iron Oxide as a PH-Dependent Indicator for Improving the Nutritional Quality. *Clin. Nutr. Res.* **2016**, *5*, 172–179. [CrossRef]
38. Veloso, C.H.; Filippov, L.O.; Filippova, I.V.; Ouvrard, S.; Araujo, A.C. Adsorption of Polymers onto Iron Oxides: Equilibrium Isotherms. *J. Mater. Res. Technol.* **2020**, *9*, 779–788. [CrossRef]
39. Bhuiyan, M.S.H.; Miah, M.Y.; Paul, S.C.; Aka, T.D.; Saha, O.; Rahaman, M.M.; Sharif, M.J.I.; Habiba, O.; Ashaduzzaman, M. Green Synthesis of Iron Oxide Nanoparticle Using Carica Papaya Leaf Extract: Application for Photocatalytic Degradation of Remazol Yellow RR Dye and Antibacterial Activity. *Heliyon* **2020**, *6*, e040603. [CrossRef]
40. Newbury, D.E. Mistakes Encountered during Automatic Peak Identification in Low Beam Energy X-ray Microanalysis. *Scanning* **2007**, *29*, 137–151. [CrossRef]
41. Liu, R.; Zhao, Y.; Huang, R.; Zhao, Y.; Zhou, H. Shape Evolution and Tunable Properties of Monodisperse Magnetite Crystals Synthesized by a Facile Surfactant-Free Hydrothermal Method. *Eur. J. Inorg. Chem.* **2010**, *2010*, 4499–4505. [CrossRef]
42. Unsoy, G.; Yalcin, S.; Khodadust, R.; Gunduz, G.; Gunduz, U. Synthesis Optimization and Characterization of Chitosan-Coated Iron Oxide Nanoparticles Produced for Biomedical Applications. *J. Nanopart. Res.* **2012**, *14*, 964. [CrossRef]
43. Wang, X.; Liu, Y.; Arandiyan, H.; Yang, H.; Bai, L.; Mujtaba, J.; Wang, Q.; Liu, S.; Sun, H. Uniform Fe_3O_4 Microflowers Hierarchical Structures Assembled with Porous Nanoplates as Superior Anode Materials for Lithium-Ion Batteries. *Appl. Surf. Sci.* **2016**, *389*, 240–246. [CrossRef]
44. Win, T.T.; Khan, S.; Bo, B.; Zada, S.; Fu, P. Green Synthesis and Characterization of Fe_3O_4 Nanoparticles Using Chlorella-K01 Extract for Potential Enhancement of Plant Growth Stimulating and Antifungal Activity. *Sci. Rep.* **2021**, *11*, 21996. [CrossRef]
45. Gautam, K.P.; Acharya, D.; Bhatta, I.; Subedi, V.; Das, M.; Neupane, S.; Kunwar, J.; Chhetri, K.; Yadav, A.P. Nickel Oxide-Incorporated Polyaniline Nanocomposites as an Efficient Electrode Material for Supercapacitor Application. *Inorganics* **2022**, *10*, 86. [CrossRef]
46. Xiang, H.; Ren, G.; Zhong, Y.; Yang, X.; Xu, D.; Zhang, Z.; Wang, X. Characterization and Synthesis of Fe_3O_4@C Nanoparticles by In-Situ Solid-Phase Method. *Mater. Res. Express* **2021**, *8*, 025016. [CrossRef]
47. Loh, K.-S.; Lee, Y.H.; Musa, A.; Salmah, A.A.; Zamri, I. Use of Fe_3O_4 Nanoparticles for Enhancement of Biosensor Response to the Herbicide 2,4-Dichlorophenoxyacetic Acid. *Sensors* **2008**, *8*, 5775–5791. [CrossRef]
48. Ardakani, L.S.; Alimardani, V.; Tamaddon, A.M.; Amani, A.M.; Taghizadeh, S. Green Synthesis of Iron-Based Nanoparticles Using Chlorophytum Comosum Leaf Extract: Methyl Orange Dye Degradation and Antimicrobial Properties. *Heliyon* **2021**, *7*, e06159. [CrossRef]
49. Eroi, N.S.; Ello, A.S.; Diabaté, D.; Koffi, K.R. Kinetic Study of the Removal of Methyl Orange Dye by Coupling WO_3/H_2O_2. *J. Chem.* **2022**, *2022*, e8633545. [CrossRef]
50. Nguyen, C.H.; Fu, C.-C.; Juang, R.-S. Degradation of Methylene Blue and Methyl Orange by Palladium-Doped TiO_2 Photocatalysis for Water Reuse: Efficiency and Degradation Pathways. *J. Clean. Prod.* **2018**, *202*, 413–427. [CrossRef]
51. Muthukumar, H.; Matheswaran, M. Amaranthus Spinosus Leaf Extract Mediated FeO Nanoparticles: Physicochemical Traits, Photocatalytic and Antioxidant Activity. *ACS Sustain. Chem. Eng.* **2015**, *3*, 3149–3156. [CrossRef]
52. Das, S.; Diyali, S.; Vinothini, G.; Perumalsamy, B.; Balakrishnan, G.; Ramasamy, T.; Dharumadurai, D.; Biswas, B. Synthesis, Morphological Analysis, Antibacterial Activity of Iron Oxide Nanoparticles and the Cytotoxic Effect on Lung Cancer Cell Line. *Heliyon* **2020**, *6*, e04953. [CrossRef] [PubMed]
53. Ismail, R.A.; Sulaiman, G.M.; Abdulrahman, S.A.; Marzoog, T.R. Antibacterial Activity of Magnetic Iron Oxide Nanoparticles Synthesized by Laser Ablation in Liquid. *Mater. Sci. Eng. C* **2015**, *53*, 286–297. [CrossRef] [PubMed]
54. Rufus, A.; Sreeju, N.; Philip, D. Synthesis of Biogenic Hematite (α-Fe_2O_3) Nanoparticles for Antibacterial and Nanofluid Applications. *RSC Adv.* **2016**, *6*, 94206–94217. [CrossRef]
55. Seddighi, N.S.; Salari, S.; Izadi, A.R. Evaluation of Antifungal Effect of Iron-oxide Nanoparticles against Different Candida Species. *IET Nanobiotechnol.* **2017**, *11*, 883. [CrossRef]

56. Caldeirão, A.C.M.; Araujo, H.C.; Tomasella, C.M.; Sampaio, C.; dos Santos Oliveira, M.J.; Ramage, G.; Pessan, J.P.; Monteiro, D.R. Effects of Antifungal Carriers Based on Chitosan-Coated Iron Oxide Nanoparticles on Microcosm Biofilms. *Antibiotics* **2021**, *10*, 588. [CrossRef]
57. Yamamoto, Y.; Imai, N.; Mashima, R.; Konaka, R.; Inoue, M.; Dunlap, W.C. Singlet Oxygen from Irradiated Titanium Dioxide and Zinc Oxide. In *Singlet Oxygen, UV-A, and Ozone*; Academic Press: Cambridge, MA, USA, 2000; Volume 319, pp. 29–37.
58. Bibi, I.; Nazar, N.; Ata, S.; Sultan, M.; Ali, A.; Abbas, A.; Jilani, K.; Kamal, S.; Sarim, F.M.; Khan, M.I.; et al. Green Synthesis of Iron Oxide Nanoparticles Using Pomegranate Seeds Extract and Photocatalytic Activity Evaluation for the Degradation of Textile Dye. *J. Mater. Res. Technol.* **2019**, *8*, 6115–6124. [CrossRef]
59. Chen, C.-Y. Photocatalytic Degradation of Azo Dye Reactive Orange 16 by TiO_2. *Water Air Soil Pollut.* **2009**, *202*, 335–342. [CrossRef]
60. Khadayat, K.; Sherpa, D.D.; Malla, K.P.; Shrestha, S.; Rana, N.; Marasini, B.P.; Khanal, S.; Rayamajhee, B.; Bhattarai, B.R.; Parajuli, N. Molecular Identification and Antimicrobial Potential of Streptomyces Species from Nepalese Soil. *Int. J. Microbiol.* **2020**, *2020*, e8817467. [CrossRef]